AGU PUBLICATIONS

Water Resources Research

RESEARCH ARTICLE
10.1002/2016WR018872

Comparative assessment of three-phase oil relative permeability models

Ehsan Ranaee[1], Monica Riva[2], Giovanni M. Porta[2], and Alberto Guadagnini[2]

[1]Dipartimento di Energia, Politecnico di Milano, Milano, Italy, [2]Dipartimento di Ingegneria Civile e Ambientale, Politecnico di Milano, Milano, Italy

Supporting Information:
• Supporting Information S1

Correspondence to:
M. Riva,
monica.riva@polimi.it

Citation:
Ranaee, E., M. Riva, G. M. Porta, and A. Guadagnini (2016), Comparative assessment of three-phase oil relative permeability models, *Water Resour. Res.*, *52*, 5341–5356, doi:10.1002/2016WR018872.

Received 2 MAR 2016
Accepted 10 JUN 2016
Accepted article online 14 JUN 2016
Published online 16 JUL 2016

Abstract We assess the ability of 11 models to reproduce three-phase oil relative permeability (k_{ro}) laboratory data obtained in a water-wet sandstone sample. We do so by considering model performance when (i) solely two-phase data are employed to render predictions of k_{ro} and (ii) two and three-phase data are jointly used for model calibration. In the latter case, a Maximum Likelihood (ML) approach is used to estimate model parameters. The tested models are selected among (i) classical models routinely employed in practical applications and implemented in commercial reservoir software and (ii) relatively recent models which are considered to allow overcoming some drawbacks of the classical formulations. Among others, the latter set of models includes the formulation recently proposed by Ranaee et al. (2015), which has been shown to embed the critical effects of hysteresis, including the reproduction of oil remobilization induced by gas injection in water-wet media. We employ formal model discrimination criteria to rank models according to their skill to reproduce the observed data and use ML Bayesian model averaging to provide model-averaged estimates (and associated uncertainty bounds) of k_{ro} by taking advantage of the diverse interpretive abilities of all models analyzed. The occurrence of elliptic regions is also analyzed for selected models in the framework of the classical fractional flow theory of displacement. Our study confirms that model outcomes based on channel flow theory and classical saturation-weighted interpolation models do not generally yield accurate reproduction of k_{ro} data, especially in the regime associated with low oil saturations, where water alternating gas injection (WAG) techniques are usually employed for enhanced oil recovery. This negative feature is not observed in the model of Ranaee et al. (2015) due to its ability to embed key effects of pore-scale phase distributions, such as hysteresis effects and cycle dependency, for modeling k_{ro} observed during WAG.

1. Introduction

Multiphase flow in porous media is inherently affected by uncertainty due to the lack of detailed knowledge of the complex physical processes involved in fluid/fluid and fluid/rock interactions. Several studies highlight the complexity of the mechanisms driving pore-scale fluid displacement in three-phase environments [e.g., *Vizika and Lombard*, 1996; *Kalaydjian et al.*, 1997; *Fenwick and Blunt*, 1998; *Blunt*, 2000; *Van Dijke and Sorbie*, 2003; *Piri and Blunt*, 2005; *Van Dijke et al.*, 2006; *Suicmez et al.*, 2007; *Sohrabi et al.*, 2008]. At the continuum (or macro) scale, the traditional depiction of multiphase flow in porous media is grounded on the Darcy-Buckingham equation where the relative phase permeability, $k_{r\alpha}$, linking the flow rate of the α fluid phase to pressure gradient, is a key parameter to estimate. Reliable experimental studies aimed at providing relative permeability data in three-phase flows are extremely complex to design and perform. An extensive and recent review on this topic is offered by *Alizadeh and Piri* [2014a]. These authors review the effect of fluid saturation, saturation history, wettability, spreading, layer drainage, and interfacial tension on $k_{r\alpha}$. While $k_{r\alpha}$ experimental data in three-phase environments are seldom available, especially in practical applications, three-phase relative permeability estimates are often obtained through empirical/semi-empirical models whose parameters are typically derived from data collected in two-phase settings. In this context, several empirical models have been proposed in the literature to characterize and predict three-phase oil relative permeability, k_{ro}. Here we consider the suite of eleven models listed in Table 1 and described in details in the Supporting Information. These models were selected among (i) classical models routinely used in practical applications and implemented in commercial reservoir software [*Stone*, 1970, 1973; *Baker*, 1988] and (ii) relatively recent and innovative models [e.g., *Jerauld*, 1997; *Delshad and Pope*, 1989; *Hustad and Hansen*,

© 2016. American Geophysical Union. All Rights Reserved.

AGU Water Resources Research

10.1002/2016WR018872

Table 1. Characteristics of the Analyzed Three-Phase Oil Relative Permeability Models Together With Results Based on Modeling Outputs Obtained by Relying Solely Upon Two-Phase Data and Making Joint Use of Two and Three-Phase Data (i.e., Obtained Through ML Parameter Estimation)

	Model Requirements for Application (Y: yes; N: no)							Model Results Obtained Through Two-Phase Data (*LMSE*)				ML Model Calibration Through Three-Phase Data ($LMSE_{min} = \hat{\sigma}_Y^2$)			
								*G*1				*G*1			
Model	Saturation of all three fluid phases	Two-phase relative permeabilities	Saturation ending points	Initial condition of the experiment	Model based on Channel flow theory	Number of model parameters (m)	Consideration of hysteresis effects	$S_{oi(1)}$ = 0.65 (n = 27)	$S_{oi(2)}$ = 0.45 (*n* = 20)	W2 (n = 17)	*All* (n = 64)	$S_{oi(1)}$ = 0.65 (*n* = 27)	$S_{oi(2)}$ = 0.45 (*n* = 20)	W2 (n = 17)	*All* (n = 64)
M_1 [*Stone*, 1970]	Y	Y	Y	N	Y	1	N	0.97	1.29	1.70	1.26	0.07	0.62	0.02	0.23
M_2 [*Stone*, 1973]	N	Y	N	N	Y	–	N	1.42	1.60	1.12	1.40	–	–	–	–
M_3 [*Delshad and Pope*, 1989]	Y	Y	Y	N	Y	6	N	0.27	1.49	0.33	0.67	0.02	0.02	0.003	0.39
M_4 [*Shahverdi and Sohrabi*, 2013]	Y	Y	Y	Y	Y	–	Y	0.33	1.02	1.01	0.91	–	–	–	–
M_5 [*Baker*, 1988]	Y	Y	Y	N	N	1	N	0.15	2.08	0.93	0.96	0.09	0.97	0.56	0.51
M_6 [*Du et al.*, 2004]	Y	Y	Y	N	N	2	N	0.18	0.18	0.54	0.28	0.16	0.21	0.14	0.11
M_7 [*Hustad and Hansen*, 1995]	Y	Y	Y	N	N	–	N	0.15	0.47	3.44	1.12	–	–	–	–
M_8 [*Blunt*, 2000]	Y	Y	Y	N	N	–	Y	0.81	0.88	0.13	0.65	–	–	–	–
M_9 [*Fenwick and Blunt*, 1998; *DiCarlo et al.*, 2000]	N	N	Y	N	N	–	N	0.13	0.56	0.15	0.27	–	–	–	–
M_{10} [*Lomeland and Ebeltoft*, 2013]	Y	Y	Y	N	N	7	N	–	–	–	–	0.02	0.003	7×10^{-4}	0.06
M_{11} [*Ranaee et al.*, 2015]	Y	Y	Y	Y	N	2 × 3	Y	0.07	0.10	0.07	0.08	0.02	0.02	0.003	0.03

1995; *Blunt*, 2000; *DiCarlo et al*., 2000; *Du et al*., 2004; *Shahverdi and Sohrabi*, 2013; *Lomeland and Ebeltoft*, 2013; *Ranaee et al*., 2015] which are considered to allow overcoming, albeit with diverse emphasis, some drawbacks of the classical formulations, as described in the following and in Supporting Information.

A first set of models ($M_1 - M_4$ in Table 1) stems from the work of *Stone* [1970] (i.e., the so-called Stone I model, M_1) and are based on channel flow theory. Model M_4 [*Shahverdi and Sohrabi*, 2013] can include hysteresis effects to characterize k_{ro} values observed during water alternating gas injection (WAG). The channel flow theory assumes that each pore is occupied by a single mobile fluid and k_{ro} at connate (or residual) water saturation $\bar{S}_{wc}$ is set equal to 1. Otherwise, numerical analyses based on pore-network modeling [e.g., *Van Dijke and Sorbie*, 2003; *Piri and Blunt*, 2005; *Van Dijke et al*., 2006; *Suicmez et al*., 2007, 2008] and experimental micromodel visualization of pore-scale fluid distribution [e.g., *Sohrabi et al*., 2008] show that more than one mobile fluid is typically found within a single pore. *Spiteri and Juanes* [2006] show that channel flow theory does not yield accurate estimates of k_{ro} for low oil saturations S_o. In particular, Stone II formulation (M_2 in this study) is prone to provide sometimes severe underestimation of k_{ro}.

A second set of models relies on a saturation-weighted interpolation between two-phase relative permeabilities (models $M_5 - M_{11}$ in Table 1). These models stem from the *Baker* [1988] formulation

$$k_{ro} = \frac{(S_w - \bar{S}_{wc})\bar{k}^I_{row} + (S_g - \bar{S}_{gt})\bar{k}^D_{rog}}{(S_w - \bar{S}_{wc}) + (S_g - \bar{S}_{gt})}, \tag{1}$$

where S_w and S_g, respectively, are water and gas saturation in the three-phase environment, $\bar{S}_{gt}$ is the saturation of trapped gas, $\bar{k}^D_{rog}$ is oil relative permeability observed during drainage in an oil-gas systems, and $\bar{k}^I_{row}$ is oil relative permeability observed during imbibition (i.e., water injection) in an oil-water system. Several studies [e.g., *Blunt*, 2000; *Spiteri and Juanes*, 2006; *Ranaee et al*., 2015] show that (1) fails in reproducing observed k_{ro} values, especially for conditions associated with low oil saturation. In this context, *Blunt* [2000] developed a relatively complex model (model M_8 in Table1) which allows (i) embedding the effect of trapping/remobilization of oil, water and gas on three-phase relative permeabilities and (ii) describing k_{ro} at very low oil saturation, corresponding to the so-called layer drainage regime. *Ranaee et al*. [2015] recently proposed to model k_{ro} through a sigmoidal function (model M_{11} in Table 1). This formulation allows reproducing (i) oil remobilization induced by gas injection in water-wet media and (ii) a smooth transition toward the layer drainage regime for low oil saturations, including (iii) the ensuing reduction of residual oil saturation in a three-phase system. *Ranaee et al*. [2015] developed two simple procedures to estimate k_{ro} during gas and water injections and assessed the strength of their approach by comparisons against two sets of laboratory-scale data (see also the Supporting Information). *Ranaee et al*. [2015] tested their model against two published data sets, which comprise a water-wet sandstone sample [*Oak*, 1990] and unconsolidated porous materials associated with diverse wettability conditions [*DiCarlo et al*., 2000].

All models listed in Table 1, with the exception of M_{10} [*Lomeland and Ebeltoft*, 2013], allow predicting k_{ro} values upon relying solely on observations performed in two-phase settings (i.e., water-oil, oil-gas, and/or water-gas) during drainage and/or imbibition, without the strict requirement of three-phase data. However, three-phase data can be used (when available) to estimate the model parameters in a number of cases, including, for example, to provide an estimate of residual oil saturation. As detailed in the Supporting Information, almost all models listed in Table 1 describe k_{ro} as a function of oil S_o, water S_w, and gas S_g saturation, i.e., saturation explicitly appears in the functional relationship employed to compute k_{ro}. The only exceptions are (i) M_2 [*Stone*, 1973], where k_{ro} depends on fluids saturation only through the corresponding value of two-phase oil relative permeability and (ii) M_9 [*Fenwick and Blunt*, 1998; *DiCarlo et al*., 2000], where k_{ro} depends only on S_o.

The diversity of models included in our analysis suggests the worth of exploring the possibility of exploiting the relative strength of each of them by employing all of them jointly within the context of a multimodel approach. The latter framework enables us to use jointly multiple models for the interpretation of observed quantities of interest. It also yields predictions, including the quantification of predictive uncertainty, by taking advantage of a suite of diverse interpretive models which can be used to characterize the system under study. The multimodel approach we consider is grounded on the Maximum Likelihood Bayesian Model Averaging (MLBMA) framework illustrated by *Neuman* [2002, 2003], *Ye et al*. [2004], and *Neuman et al*. [2012]. While applications of multimodel approaches in subsurface environments have mostly studied flow

behavior in porous and/or fractured media, with limited analysis of conservative and reactive transport [see, e.g., *Ciriello et al*., 2013, 2015, and references therein], the analysis of the potential of the approach to complex settings of the kind encountered in the characterization of three-phase relative permeabilities has not yet been explored.

In this work, we present a detailed analysis of the capability of models $M_1 - M_{11}$ to characterize and predict observed three-phase oil relative permeabilities. We do so by considering as a test bed the recent high-quality three-phase oil relative permeability data set described by *Alizadeh and Piri* [2014b] and acquired on water-wet consolidated Bentheimer sandstone under steady state conditions. In section 3.1, we estimate k_{ro} by only using the two-phase data provided by *Alizadeh and Piri* [2014b]. As indicated in Table 1, six models (M_1, M_3, M_5, M_6, M_{10}, and M_{11}) include parameters that can also be estimated upon relying directly on three-phase oil relative permeability data. We do so by applying the Maximum Likelihood (ML) approach briefly described in section 2.1. Then we treat the models considered as a set of competing alternatives, rank them through model selection (or model discrimination) criteria, and evaluate the posterior probability (or weight) associated with each model. Finally, we assess the posterior mean and variance of k_{ro} by considering all models jointly within the framework of a multimodel analysis approach. Key results are summarized in section 3 which also includes a comparative analysis of the elliptic regions, i.e., regions where the flow problem becomes ill posed [e.g., *Trangenstein*, 1989; *Shearer and Trangenstein*, 1989; *Jackson and Blunt*, 2002; *Juanes and Patzek*, 2004; *Bianchi Janetti et al*., 2015], that can occur for selected models.

2. Methodology

2.1. Maximum Likelihood Calibration and Model Discrimination Criteria

As mentioned in section 1, six of the models listed in Table 1 can be calibrated by making use of available three-phase relative permeability data. Table 1 lists the number of parameters (m) to be estimated for each of these models (see also Supporting Information for additional details). In the following we briefly summarize the Maximum Likelihood (ML) procedure used in section 3 to estimate model parameters and associated bounds of uncertainty. Then we describe the model selection criteria we apply to (i) rank diverse models and (ii) obtain multimodel predictions through ML Bayesian Model Averaging (MLBMA).

We introduce the vector $\mathbf{Y}$ whose entries are n true values of $Y_i = \log k_{ro}(S_{o,i}) = \log k_{ro,i}$, with $i = 1,\ldots n$, and the vector $\mathbf{Y}^*$ containing n available noisy measurements of Y_i, $Y_i^* = \log k_{ro,i}^*$. We treat the prior measurement error vector $\boldsymbol{\varepsilon} = \mathbf{Y} - \mathbf{Y}^*$ as being multivariate Gaussian. A maximum likelihood estimate $\hat{\boldsymbol{\theta}}$ of the parameter vector $\boldsymbol{\theta}$ of size m can be obtained by minimizing the negative log likelihood criterion (NLL) [*Carrera and Neuman*, 1986]

$$NLL = \frac{J}{\sigma_Y^2} + n \ln(2\pi\sigma_Y^2), \tag{2}$$

with respect to $\boldsymbol{\theta}$, where σ_Y^2 represents the measurement error variance. Here we assume error measurements to be uncorrelated and their statistics to be uniform. Therefore, the covariance matrix of measurement errors $\mathbf{C}_Y$ can be written as $\mathbf{C}_Y = \sigma_Y^2 \mathbf{I}$, $\mathbf{I}$ being the identity matrix. The quantity J in (2) is equivalent to the least square criterion

$$J = \sum_{i=1}^{n} \varepsilon_i^2 \quad \text{with} \quad \varepsilon_i = Y_i - Y_i^*, \tag{3}$$

where Y_i are evaluated according to models M_1 (with $m = 1$), M_3 (with $m = 6$), M_5 (with $m = 1$), M_6 (with $m = 2$), M_{10} (with $m = 7$), and M_{11} (with $m = 2$). Note that σ_Y^2 is generally unknown and the ML estimate of σ_Y^2 can be obtained as

$$\hat{\sigma}_Y^2 = \frac{J_{\min}}{n}. \tag{4}$$

$J_{\min}$ being the minimum value of J, i.e., $J_{\min} = J(\hat{\boldsymbol{\theta}})$. The covariance matrix of the estimation error is approximated by its Cramer-Rao lower bound as

$$\mathbf{Q}=\hat{\sigma}_Y^2\left(\mathbf{J}^T\mathbf{J}\right)^{-1}, \tag{5}$$

where the superscript T denotes transpose and $\mathbf{J}$ is the $n \times m$ Jacobian matrix whose entries are the derivatives of the target variable, Y_i, with respect to the model parameters evaluated at $\hat{\boldsymbol{\theta}}$. Approximation (5) obviates calculation of second-order derivatives of *NLL* (2). The diagonal entries of $\mathbf{Q}$ provide lower bound estimates of parameter estimation variance. In this work, minimization of (3) is achieved through the gradient method [e.g., *Nocedal and Wright*, 2006], as implemented in the Matlab environment.

Various model information (known also as model selection or discrimination) criteria *IC* have been proposed in the literature to discriminate among models which are formulated with the aim of interpreting a target quantity of interest. These include the information criterion AIC_c [*Hurvich and Tsai*, 1989] and the Bayesian criteria *BIC* [*Schwarz*, 1978] and *KIC* [*Kashyap*, 1982], respectively defined as

$$AIC_c=NLL+2m+\frac{2m(m+1)}{n-m-1}, \tag{6}$$

$$BIC=NLL+m\ \ln n, \tag{7}$$

$$KIC=NLL-m\ \ln(2\pi)-\ln|\mathbf{Q}|. \tag{8}$$

All these criteria consider the goodness of fit between available measurements and ML estimates (through *NLL*) and tend to penalize models with a large number of parameters (parsimony principle). *KIC* also includes a quantitative metric of the quality of the parameter estimates, as rendered by $|\mathbf{Q}|$, as an additional term assisting in discriminating among model performance. AIC_c tends to select more complex models as n increases while *KIC* reduces to *BIC* when $n \gg m$ (see, e.g., *Ye et al*. [2008] for a detailed discussion on these points). In the context of nonlinear geostatistical inverse problems of single-phase flow in porous media, *Ye et al*. [2008] and *Riva et al*. [2011] demonstrated the unique ability of *KIC* to estimate the parameters of the variogram of randomly heterogeneous log conductivity fields.

Maximum Likelihood Bayesian Model averaging (MLBMA) [*Neuman*, 2003; *Ye et al*., 2004] stands out as a robust and computationally efficient way to combine the predictive capabilities of a suite of distinct models. Following *Neuman* [2003], the posterior model weight (for AIC_c) or the posterior model probability (for *BIC* and *KIC*) of model M_k comprised in the collection of N_M candidate models analyzed is given by

$$p(M_k|\mathbf{Y}^*)=\frac{\exp\left(-{}^1\!/_2\Delta IC_k\right)p(M_k)}{\sum_{i=1}^{N_M}\exp\left(-{}^1\!/_2\Delta IC_i\right)p(M_i)}. \tag{9}$$

Here IC_k is any criterion from (6)–(8), $\Delta IC_k=IC_k-IC_{\min}$ with $IC_{\min}=\min\{IC_k\}$ evaluated over all N_M competing models and $p(M_k)$ is the prior probability of model M_k. The multimodel posterior mean and variance of $\mathbf{Y}$ are, respectively, evaluated as

$$E(\mathbf{Y}|\mathbf{Y}^*)=\sum_{k=1}^{N_M}E(\mathbf{Y}|\mathbf{Y}^*,M_k)p(M_k|\mathbf{Y}^*), \tag{10}$$

$$Var(\mathbf{Y}|\mathbf{Y}^*)=\sum_{k=1}^{N_M}Var(\mathbf{Y}|\mathbf{Y}^*,M_k)p(M_k|\mathbf{Y}^*)+\sum_{k=1}^{N_M}\left[E(\mathbf{Y}|\mathbf{Y}^*,M_k)-E(\mathbf{Y}|\mathbf{Y}^*)\right]^2p(M_k|\mathbf{Y}^*). \tag{11}$$

$E(\mathbf{Y}|\mathbf{Y}^*,M_k)$ and $Var(\mathbf{Y}|\mathbf{Y}^*,M_k)$, respectively, being the posterior mean and variance of $\mathbf{Y}$ computed for model M_k. We provide the application of MLBMA to our suite of multiple models in section 3.2.

2.2. Analysis of Elliptic Regions

In section 3, we investigate the possibility of occurrence of elliptic regions, as embedded in the classical fractional-flow theory of displacements [*Jackson and Blunt*, 2002], in (i) two classical models typically used in black-oil reservoir simulators (i.e., the Stone I and Baker models, respectively, identified as M_1 and M_5 in Table 1) and (ii) the very recent sigmoid-based model presented by *Ranaee et al*. [2015] (model M_{11} in Table 1). The analysis of elliptic regions is critical to modeling of three-phase flows at the macro- (Darcy-) scale because the flow problem becomes ill posed for saturations at which the governing system of equations is elliptic.

Darcy-scale three-phase flow of immiscible and incompressible fluids in a porous medium in one dimension is governed by

$$\partial_t \mathbf{u} + \partial_x \mathbf{f} = 0 \quad \text{with} \quad \mathbf{u} := \begin{Bmatrix} S_g \\ S_w \end{Bmatrix}; \ \mathbf{f} := \begin{Bmatrix} f_g \\ f_w \end{Bmatrix}, \tag{12}$$

where f_w and f_g, respectively, are the fractional flows of water and gas phases and x and t are rescaled space and time variables. If gravity and capillary forces are neglected, fractional flow of each phase is defined as the phase mobility ratio ($\lambda_\alpha = k_{r\alpha}/\mu_\alpha$ with $\alpha = w, g$; μ_α being the dynamic viscosity of the α-phase) divided by the total mobility ratio, $\lambda_T = \lambda_w + \lambda_o + \lambda_g$. In the following, we focus our study on the occurrence of elliptic regions associated with k_{ro} models. Thus, we neglect hysteresis effects in the prediction of water (k_{rw}) and gas (k_{rg}) relative permeabilities. The latter are, respectively, approximated by water ($\bar{k}^I_{rwo}$) and gas ($\bar{k}^I_{rgo}$) relative permeabilities in two-phase (oil-water and oil-gas) systems under imbibition [*Corey and Rathjens*, 1956], i.e.,

$$k_{rw} \approx \bar{k}^I_{rwo} = \bar{k}^M_{rwo} \left(\frac{\bar{S}_{wo} - \bar{S}_{wc}}{1 - \bar{S}_{wc}} \right)^{ewo}, \tag{13}$$

$$k_{rg} \approx \bar{k}^I_{rgo} = \bar{k}^M_{rgo} \left(\frac{\bar{S}_{go} - \bar{S}_{gt}}{1 - \bar{S}_{wc} - \bar{S}_{rog} - \bar{S}_{gt}} \right)^{ego}. \tag{14}$$

$\bar{k}^M_{rwo}$ and $\bar{k}^M_{rgo}$, respectively, being the maximum water and gas relative permeabilities in two-phase environments. Here $\bar{S}_{wo}$ is water saturation in oil-water systems, $\bar{S}_{go}$ and $\bar{S}_{rog}$, respectively, are gas and residual oil saturation in oil-gas systems, and *ewo* and *ego* are model parameters. The latter are here obtained through ML estimation on the basis of the two-phase relative permeability data of *Alizadeh and Piri* [2014b] (see also section 3.1). All remaining quantities have been defined above.

When gravity and capillarity effects are considered, the fractional flows can be evaluated as [*Juanes and Patzek*, 2004; *Bianchi Janetti et al.*, 2015]

$$f_w = \frac{\lambda_w}{\lambda_T} \left[1 - N_d \mu_o (\rho_d - 1) \lambda_o + \rho_d \lambda_g \right], \tag{15}$$

$$f_g = \frac{\lambda_g}{\lambda_T} \left[1 + N_d \mu_o (\rho_d \lambda_w + \lambda_o) \right], \tag{16}$$

where $\rho_d = (\rho_w - \rho_g)/(\rho_o - \rho_g)$ is the density ratio and $N_d = (\rho_0 - \rho_g) K g_x / (\mu_o q \phi)$ is the gravity number, ρ_α being density of fluid phase α; K, ϕ, g_x, and q are intrinsic permeability and porosity of the medium, the component of gravity along the flow direction and the total volumetric flow rate. The nature of (12) can be determined by analyzing the behavior of the eigenvalue problem

$$\mathbf{A}\mathbf{r} = v\mathbf{r} \quad with \quad \mathbf{A} = \begin{bmatrix} a & b \\ c & d \end{bmatrix} = \begin{bmatrix} \partial f_g / \partial S_g & \partial f_g / \partial S_w \\ \partial f_w / \partial S_g & \partial f_w / \partial S_w \end{bmatrix}, \tag{17}$$

where $\mathbf{A}$ is the Jacobian matrix of (12), v is an eigenvalue, and $\mathbf{r} = \left[r_{i,Sg}, r_{i,Sw} \right]^T$ ($i = 1, 2$) is a right eigenvector. The eigenvalues $v_{1,2}$ and $\mathbf{r}$ are evaluated as

$$v_{1,2} = \frac{1}{2} \left[a + d \pm \sqrt{(a-d)^2 + 4bc} \right], \tag{18}$$

$$\frac{r_{1,Sg}}{r_{1,Sw}} = \frac{v_1 - a}{b} = \frac{c}{v_1 - d}, \frac{r_{2,Sg}}{r_{2,Sw}} = \frac{b}{v_2 - a} = \frac{v_2 - d}{c}. \tag{19}$$

For any combination of S_g and S_w, the system (12) is elliptic when $v_{1,2}$ are complex conjugates. Regions identified in the saturation space to correspond to this state are termed elliptic regions. When $v_{1,2}$ are real and distinct, the system (12) is hyperbolic and $v_{1,2}$ represent the characteristic speed at which waves describing changes in saturation propagate throughout the domain. In this case, there are two real and linearly independent eigenvectors that, when viewed in the saturations space, correspond to the directions of admissible changes in fluid saturations and identify so called fast and slow rarefaction curves.

3. Results

In this section, we assess the capability of the collection of models listed in Table 1 to characterize and predict three-phase oil relative permeability data. We do so by grounding our study on the data presented by *Alizadeh and Piri* [2014b]. These authors provide oil relative permeability data under steady state conditions during two- (gas/oil, oil/brine, and gas/brine) and three-phase (gas/oil/brine) coreflooding experiments in (water-wet) Bentheimer sandstone core samples. The data set presented by the authors include experiments of primary gas injection (*G*1 in Table 1) performed with two initial oil saturations ($S_{oi(1)}=65\%$ and $S_{oi(2)}=45\%$) followed by the waterflooding experiments (*W*2 in Table 1), representing the behavior of oil relative permeability k_{ro} under a WAG cycle. The data set of *Alizadeh and Piri* [2014b] is here classified as follows (see Table 1 for nomenclature, which we employ hereinafter):

1. Data set *G*1 with $S_{oi(1)}=65\%$ comprises 8 data points from experiment A and 12 data points from experiment B.
2. Data set *G*1 with $S_{oi(2)}=45\%$ comprises three sets of nine data points, respectively, associated with experiments C, E, and G.
3. Data set *W*2 includes all data points for which decreasing gas saturation is reported, i.e., nine points from experiment A and eight points from experiment F.

Note that from each experiment we select only data corresponding to three-phase flow (i.e., all three fluid saturations are larger than zero) and for which $k_{ro}>0$. *Alizadeh and Piri* [2014b, Experiment D-1] is associated with measurements performed in a gas-oil environment at connate water saturation. Following a common practice [e.g., *Spiteri and Juanes*, 2006], we employ experiment D-1 to characterize the two-phase oil relative permeability $\bar{k}^D_{rog}$.

3.1. Predictions of k_{ro} Relying Only on Two-Phase Data

We estimate k_{ro} in all three settings (e.g., *G*1 with $S_{oi(1)}$, *G*1 with $S_{oi(2)}$, and *W*2) considered by *Alizadeh and Piri* [2014b] by relying only on their two-phase data and applying all models listed in Table 1. We do not consider in this analysis model M_{10}, whose parameters need to be estimated on the basis of three-phase data (see Supporting Information for details). When needed (i.e., for M_1, M_3, M_4, and M_5), we evaluate residual oil saturation S_{or} by making use of (S3). The need for a proper estimate of S_{or} to accurately predict k_{ro} has been recently discussed by *Kianinejad et al.* [2015] and *Kianinejad and DiCarlo* [2016]. Note that M_{11} requires estimating two distinct parameters for each of the three settings (see also Supporting Information).

Table 1 lists the values of $LMSE=J/n$, where J is calculated according to (3) and n is the number of experimental data available, resulting by considering each of the three experimental sets individually and merging all data into a unique data set. We note that M_{11} [*Ranaee et al.*, 2015] renders the smallest *LMSE* values for all three sets of experiments, followed by M_6, M_8, or M_9 (in an order which depends on the setting analyzed). This high-quality performance of M_{11}, as quantified in terms of *LMSE* values, with respect to the other investigated models can be due to its inherent capability of embedding (i) impact of hysteresis, due to the two diverse strategies developed for the prediction of k_{ro} under gas injection or waterflooding, and (ii) cycle dependency effects, because the model directly considers the influence of initial oil saturation and/or the initialization of the experiment (see Supporting Information for details).

As an example, Figure 1 depicts the graphical comparison among three-phase oil relative permeabilities predicted by two of the models which are commonly implemented in commercial software (M_1 and M_5) and those obtained by M_4 and M_{11}, together with experimental data. The Baker model (M_5) yields quite good predictions of k_{ro} data collected during gas injection when initial oil saturation is high (see Figure 1a). These results are explained upon observing that values of $\bar{k}^I_{row}$, $\bar{k}^D_{rog}$, and k_{ro} are very similar for high S_{oi} values, so that all saturation-weighted interpolation models lead to acceptable results under these conditions. Moreover, differences between displacement of oil under gas and water injection are very limited when S_{oi} is large (this condition corresponding to piston-type configuration [*Piri and Blunt*, 2005]), and saturation-weighted interpolation-based models that do not account for hysteresis effects can be successfully employed in this regime. The Baker model fails in reproducing experimental data associated with gas injection and small initial oil saturation values (see Figure 1b), a condition for which WAG techniques are usually employed. The general underestimation of k_{ro} obtained with M_5 in these conditions is likely linked to the observation that the coexistence of a considerable amount of all three phases in the system tends to

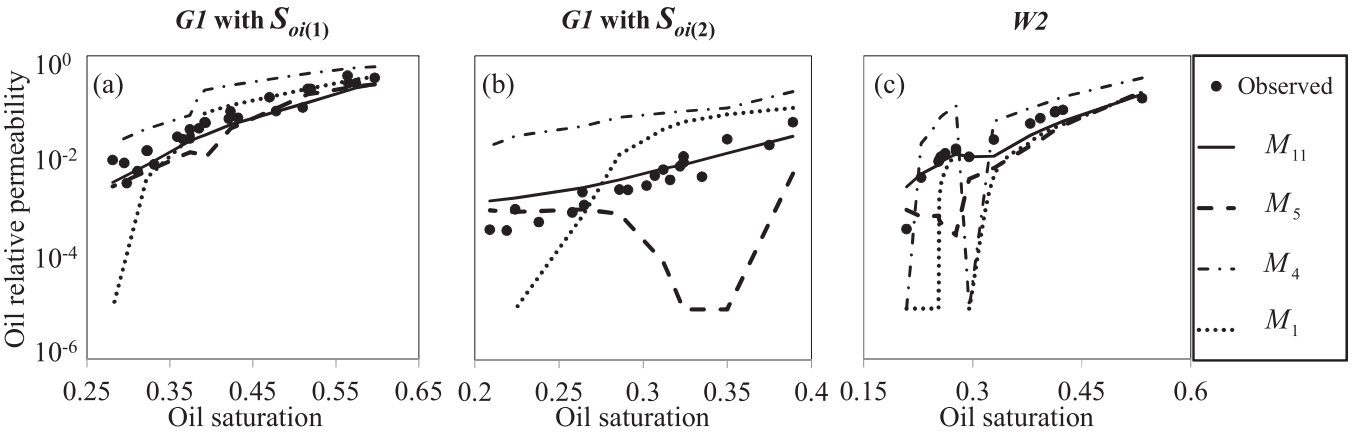

Figure 1. Three-phase oil relative permeability versus oil saturation. Curves represent values calculated through models M_1, M_4, M_5, and M_{11} based solely on information from two-phase data. Figures 1a and 1b include analysis of experiments performed following primary gas injection; Figure 1c considers secondary waterflooding experiments.

increase the occurrence of oil remobilization from small pores through spreading layers [*Suicmez et al.*, 2007, 2008]. Additionally, one should note that $\bar{k}^I_{row}$ vanishes for $S_o < \bar{S}_{row}$ and by using (1) leads to k_{ro} values which are slightly smaller than $\bar{k}^D_{rog}$. This result is in contrast with experimental coreflooding observations [e.g., *Oak*, 1990; *DiCarlo et al.*, 2000; *Alizadeh and Piri*, 2014b] showing that oil recovery increases shifting from two to three-phase environments. Similar to what observed above for M_{11}, also the saturation-weighted interpolation-based models $M_6 - M_9$ are associated with values of k_{ro} under gas injection experiments initiated in low oil saturations (*G*1 data set with $S_{oi} = 0.45$) of relatively improved quality with respect to the Baker model (see Table 1). This results is consistent with the observations that (i) M_6 and M_7 are characterized by an increased weight of $\bar{k}^D_{rog}$ since they disregard the effect of trapped gas, (ii) M_8 considers remobilization of oil under layer drainage configurations, and (iii) M_9 somehow takes into account nonlinear variations of k_{ro} with S_o at low oil saturations.

The models based on the channel flow theory ($M_1 - M_4$) generally do not accurately reproduce the k_{ro} data considered. In particular, model M_1 tends to overestimate k_{ro} for high oil saturations and to underestimate k_{ro} when S_o decreases (see Figures 1a and 1b). This result can be explained upon noting that M_1 requires the use of $\bar{k}^I_{row}$ and $\bar{k}^D_{rog}$ values evaluated for oil saturation levels different from those observed under three-phase environments (see section S1 of the Supporting Information), a similar consideration holding also for M_2 and M_4. Figure 1 shows that M_4, which includes hysteresis effects, tends to overestimate k_{ro}. This is consistent with the observation that M_4 was developed on the basis of data collected in the presence of low interfacial tension, where oil relative permeability tends to be relatively large [*Harbert*, 1983; *Fatemi et al.*, 2011; *Chukwudeme et al.*, 2014].

3.2. ML Estimate of k_{ro} Based on Three and Two-Phase Data

For six (M_1, M_3, M_5, M_6, M_{10}, and M_{11}) of the 11 models analyzed, it is possible to constrain model parameters through the use of available three-phase oil relative permeability data. We do so by applying the approach described in section 2 to compute ML estimates of model parameters. Results of this analysis are listed in Table 1 in terms of $LMSE_{\min} = J_{\min}/n = \hat{\sigma}^2_Y$, as given by (4). Similar to what has been presented in section 3.1, $LMSE_{\min}$ has been evaluated by considering each of the three experimental sets individually and merging all data into a unique data set. As expected, values of $LMSE_{\min}$ for M_1, M_3, M_5, M_6, and M_{11} are generally smaller than those of the corresponding *LMSE* since three-phase data are considered in the model calibration procedure. We note that $0.01 < LMSE_{min}/LMSE < 0.6$ (depending on the model and experimental setting considered) for models M_1 and M_5, where only residual oil saturation is calibrated. This type of result is in agreement with the main findings of *Kianinejad et al.* [2015].

Figure 2 provides a graphical depiction of three-phase experimental data and the corresponding ML estimates of k_{ro} (i.e., k_{ro} computed with the ML estimate $\hat{\boldsymbol{\theta}}$ of the parameter vector $\boldsymbol{\theta}$) based on M_1, M_3, M_{10}, and M_{11} for the three experimental scenarios considered. Comparison of Figures 1 and 2 evidences the general improvement in the quality of model results emerging from constraining model parameters through ML calibration on three-phase data.

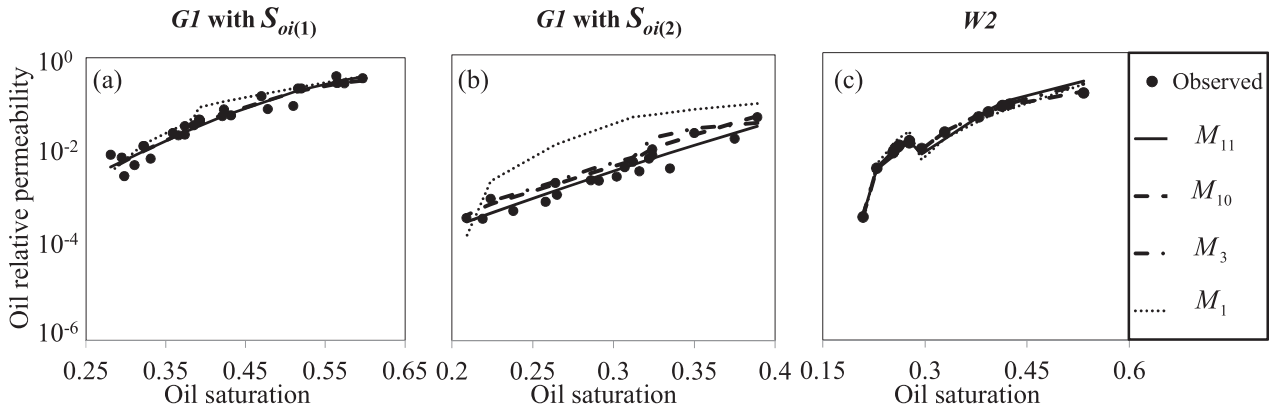

Figure 2. ML estimates of three-phase oil relative permeability versus oil saturation for models M_1, M_3, M_{10}, and M_{11} and are based on information from two and three-phase data. Figures 2a and 2b include analysis of experiments performed following primary gas injection; Figure 2c considers secondary waterflooding experiments.

When all available data are jointly considered in the ML analysis, models M_{10} and M_{11} provide the smallest values of $LMSE_{\min}$, equal to 0.06 and 0.03, respectively (see Table 1). Remarkably, calibrated models M_1, M_3, M_5, and M_6 are seen to be associated with values of $LMSE_{\min} > 0.08$, the latter being the value of *LMSE* associated with M_{11} when solely two-phase data are employed (see section 3.1), i.e., without model calibration. In other words, model M_{11} is conducive to estimates of k_{ro} of higher quality (when assessed in terms of *LMSE*) than those rendered by all other tested models, even in cases where three-phase data are included in these and are not considered in M_{11}. This result provides evidence of the superior predictive capability of M_{11} in the settings analyzed. Figure 3 shows estimates of k_{ro} obtained with a set of models upon (a) relying only on two-phase data (Figure 3a) or (b) making also use of three-phase data (Figure 3b) versus all (*G*1 and *W*2) experimental data considered jointly. These results allow appreciating the generally superior performance of M_{11} in reproducing k_{ro}, as compared to all other models considered.

Figure 4 depicts the values of the model selection criteria (*IC*s) (6)–(8) for each model. Models M_3, M_{10}, and M_{11} are identified as best depending on the experimental setting (Figures 4a–4c) and the model discrimination criterion, *IC*, adopted. Model M_{11} is unambiguously selected as the best model by all *IC*s when all data are jointly considered (see Figure 4d). The latter finding can be explained upon considering the structure of models M_3 and M_{10}. In particular, these models do not consider (i) the impact of initialization of phase saturations at the onset of each experiment (cycle dependency) and (ii) hysteresis effects yielding differences in the system and model behavior under gas injection and water flooding scenarios, while M_{11} is designed to embed these physical features.

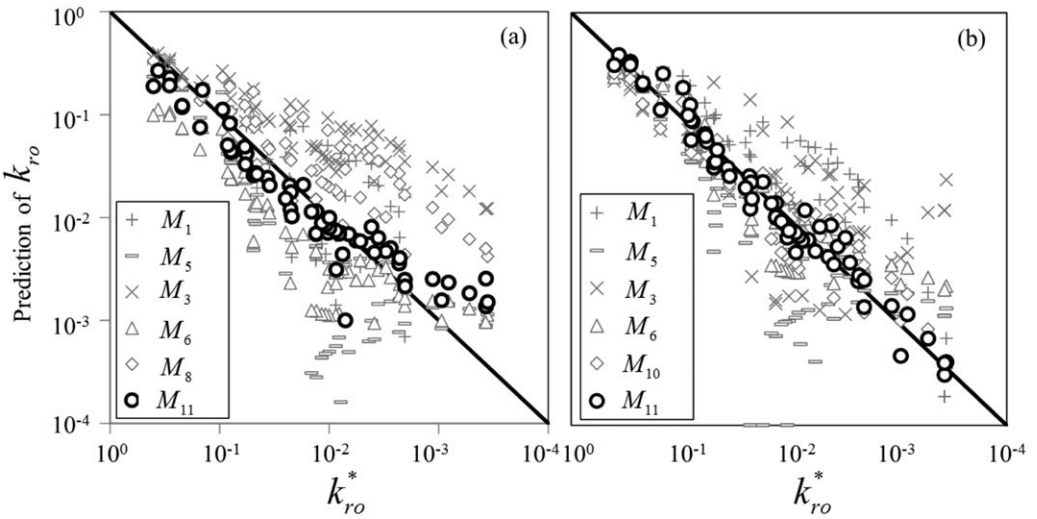

Figure 3. Estimates of k_{ro} obtained (a) relying only on two-phase and (b) making also use of three-phase data, versus experimental values (data from primary gas injection and secondary waterflooding are jointly considered).

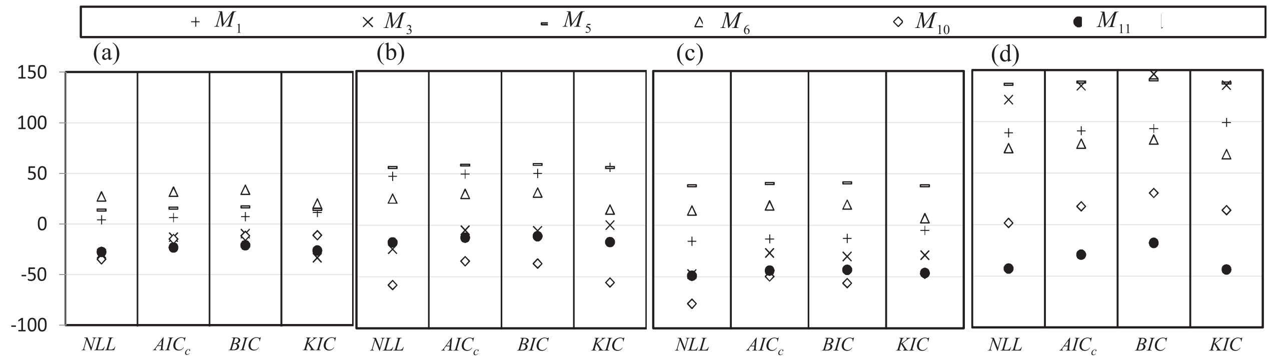

Figure 4. Model selection criteria evaluated on the basis of ML calibration of models M_1, M_3, M_5, M_6, M_{10}, and M_{11} on the three-phase oil relative permeability data obtained under primary gas injection (*G*1) with initiation at (a) high $S_{oi(1)}$ and (b) low $S_{oi(2)}$ oil saturations; (c) secondary waterflooding (*W*2); and (d) complete data set (*G*1 + *W*2 experiments).

We then evaluate the posterior model weight (for AIC_c) or the posterior model probability (for *BIC* and *KIC*), $p(M_k|\mathbf{Y}^*)$, according to (9) for each candidate model and for each model *IC*, including *NLL* as a term of comparison. We assign an equal prior probability $p(M_k)=1/6=16.7\%$ to each model ($k=1, 3, 5, 6, 10, 11$). Table 2 lists these results for M_3, M_{10}, and M_{11} (M_1, M_5, and M_6 are associated with virtually zero posterior probabilities). In all cases, $p(M_k|\mathbf{Y}^*)$ is markedly different from the prior probability, reflecting the relevant impact of conditioning on the available three-phase data. The value of $p(M_k|\mathbf{Y}^*)$ associated with M_{11} is equal to 1 when all data are jointly considered, independent of the discrimination criterion adopted. Model M_{10} is assigned (a) a unit weight when only *G*1 experiments initiated with low oil saturation ($S_{oi(2)}$) are considered and (b) the largest weight for experiments *W*2 according to all model discrimination criteria.

Interpretation of the results of experiments *G*1 initiated with large oil saturation ($S_{oi(1)}$) is not straightforward. While M_{10} provides the best match against the data (as quantify by *NLL*), AIC_c and *BIC* favor M_{11} (with $p(M_k|\mathbf{Y}^*)$, respectively, equal to 97.8 and 98.8%), and *KIC* selects M_3 ($p(M_k|\mathbf{Y}^*)$ equal to 97.2%) as best model. This difference between model rankings stems from the characteristics of the diverse model information criteria analyzed. We start by noting that M_3, M_{10}, and M_{11} lead to very similar results in this case (see Figure 2a). Therefore, while *NLL* (that considers only the quality of the fit) tends to prefer the model with the largest number of parameters (i.e., M_{10}, with $m=7$), AIC_c and *BIC* favor the model with the smallest m value (i.e., M_{11}, with $m=2$). As discussed in section 2.1, *KIC* also includes a metric quantifying the quality of the parameter estimate as discriminant among models. Figure 5 depicts uncertainty bounds, as quantified by $(\hat{\theta}+\hat{\sigma}_\theta)/\hat{\theta}$, $\hat{\sigma}_\theta$ being the square root of the parameter estimation error variance, associated with each estimated parameter of models M_3, M_{10}, and M_{11}. We note that the ML estimate of θ_5 of M_3 obtained for *G*1 with initial large oil saturation ($S_{oi(1)}$) is associated with a large estimation uncertainty (see Figure 5a), consistent with *KIC* favoring M_3 in this case. We further note that according to *Tsai and Li* [2008] *BIC* should be preferred to *KIC* when comparing models embedding considerably different types of characteristic uncertain parameters, as is the case here.

Finally, we apply MLBMA to provide a multimodel analysis of the oil relative permeability data. We do so by (i) selecting a model M_k (with $k=3$, 10, or 11); (ii) generating $NMC=10^7$ Monte Carlo (MC) realizations of each model parameter θ_i (with $i=1,\ldots,m$), assuming the estimation error associated with θ_i to be Gaussian with mean and variance respectively given by $\hat{\theta}_i$ and $\hat{\sigma}_{\theta_i}$; (iii) use model M_k to obtain $NMC=10^7$ MC realizations of $\mathbf{Y}$; (iv) computing mean, $E(\mathbf{Y}|\mathbf{Y}^*, M_k)$, and variance, $Var(\mathbf{Y}|\mathbf{Y}^*, M_k)$, of $\mathbf{Y}$ across realizations evaluated

Table 2. Posterior Weights/Probability Calculated From (9) Using *NLL* (2), AIC_c (6), *BIC* (7), and *KIC* (8) for Candidate Models M_3, M_{10}, and M_{11}

	Posterior Model Weight Based on *NLL*				Posterior Model Weight Based on AIC_c				Posterior Model Probability Based on *BIC*				Posterior Model Weight Based on *KIC*			
	G1				G1				G1				G1			
Model	$S_{oi(1)}=0.65$ ($n=27$)	$S_{oi(2)}=0.45$ ($n=20$)	*W*2 ($n=17$)	*All* ($n=64$)	$S_{oi(1)}=0.65$ ($n=27$)	$S_{oi(2)}=0.45$ ($n=20$)	*W*2 ($n=17$)	*All* ($n=64$)	$S_{oi(1)}=0.65$ ($n=27$)	$S_{oi(2)}=0.45$ ($n=20$)	*W*2 ($n=17$)	*All* ($n=64$)	$S_{oi(1)}=0.65$ ($n=27$)	$S_{oi(2)}=0.45$ ($n=20$)	*W*2 ($n=17$)	*All* ($n=64$)
M_3	5.6%	0%	0%	0%	0.6%	0%	0%	0%	0.3%	0%	0%	0%	97.2%	0%	0%	0%
M_{10}	91.8%	100%	100%	0%	1.6%	100%	94.4%	0%	0.9%	100%	100%	0%	0%	100%	59.4%	0%
M_{11}	2.6%	0%	0%	100%	97.8%	0%	5.6%	100%	98.8%	0%	0%	100%	2.8%	0%	40.6%	100%

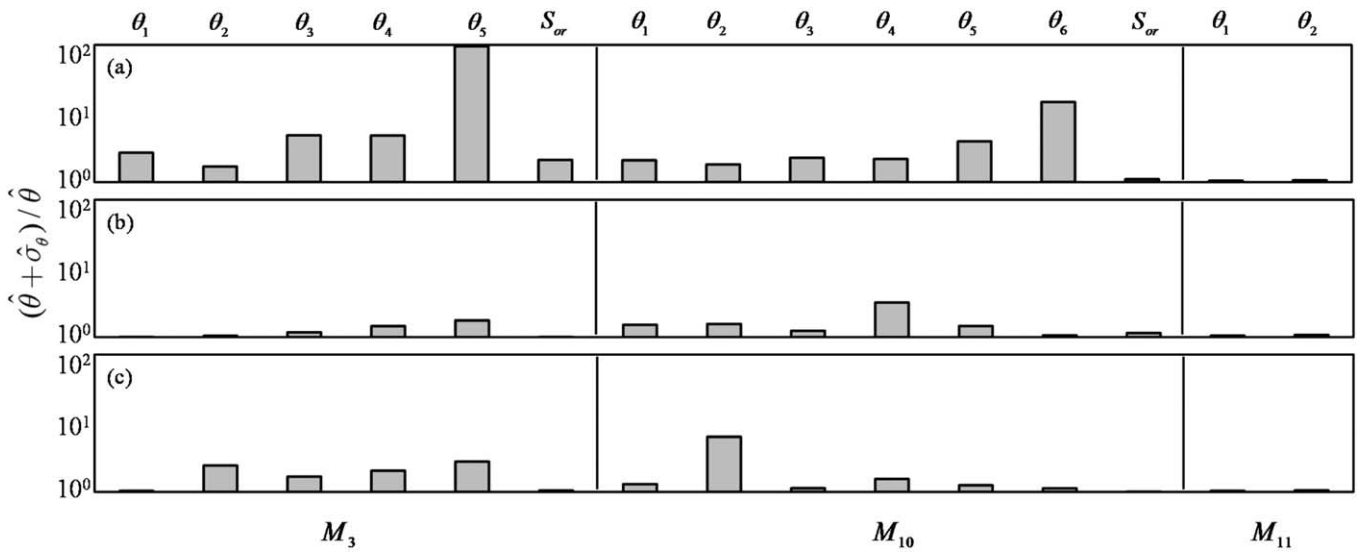

Figure 5. Normalized uncertainty bounds, as quantified by $(\hat{\theta}+\hat{\sigma}_\theta)/\hat{\theta}$, for all parameter estimates $\hat{\theta}$ resulting from ML calibration of models M_3, M_{10}, and M_{11}; experiments *G*1 initiated with (a) $S_{oi(1)}$ and (b) $S_{oi(2)}$; (c) experiment *W*2.

at step (iii); and (v) use (10) and (11) to compute MLBMA estimates $E(\mathbf{Y}|\mathbf{Y}^*)$ and variance $Var(\mathbf{Y}|\mathbf{Y}^*)$. Figure 6 depicts a scatterplot of MLBMA estimates, $E(\mathbf{Y}|\mathbf{Y}^*)$, versus observed three-phase oil relative permeabilities, log k_{ro}^*, for experiments *G*1 with $S_{oi(1)}$ and replacing *IC* in (9)–(11) with *NLL* (Figure 6a), AIC_c (Figure 6b), *BIC*

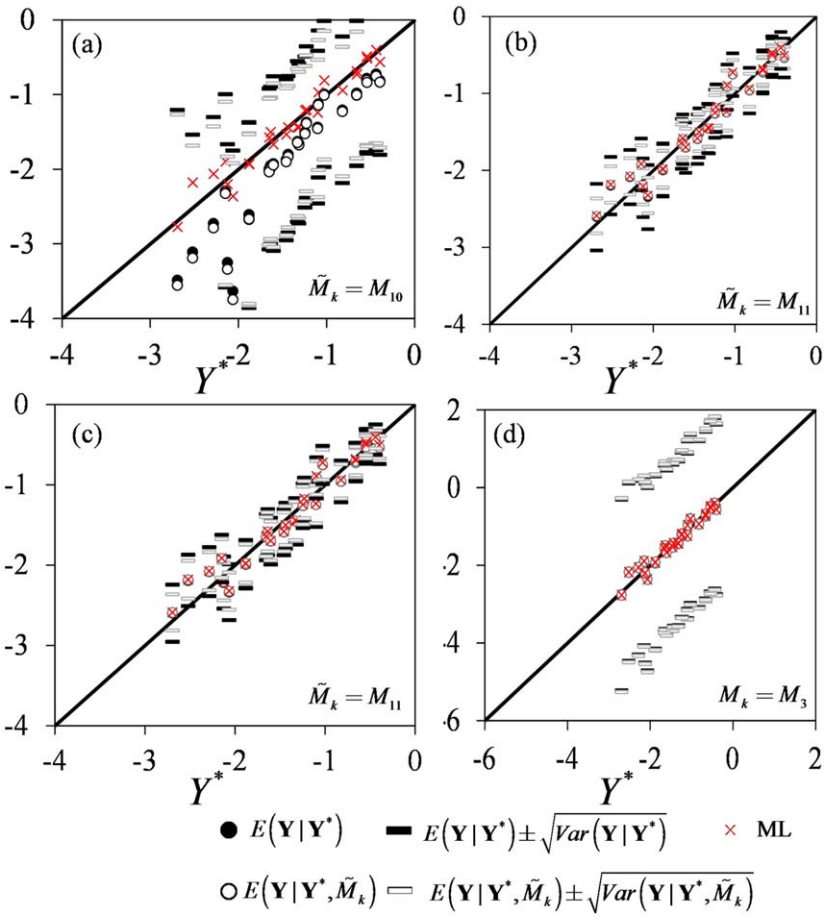

Figure 6. Estimates of k_{ro} versus experimental values observed during *G*1 with $S_{oi(1)}$ and *IC* = (a) *NLL*; (b) AIC_c; (c) *BIC*; and (d) *KIC*.

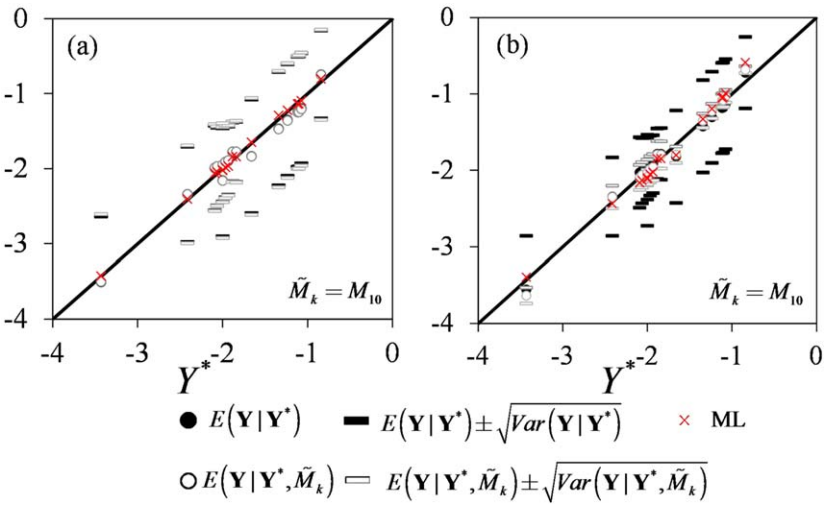

Figure 7. Estimates of k_{ro} versus experimental values observed during *W*2 and *IC* = (a) AIC_c and (b) *KIC*.

(Figure 6c), and *KIC* (Figure 6d). As an additional term of comparison, Figure 6 also depicts intervals of width $E(\mathbf{Y}|\mathbf{Y}^*) \pm \sqrt{Var(\mathbf{Y}|\mathbf{Y}^*)}$, characterizing the uncertainty associated with MLBMA estimates. To highlight the relevance of the uncertainty associated with a given model, Figure 6 includes values of $E(\mathbf{Y}|\mathbf{Y}^*, \tilde{M}_k)$ and $E(\mathbf{Y}|\mathbf{Y}^*, \tilde{M}_k) \pm \sqrt{Var(\mathbf{Y}|\mathbf{Y}^*, \tilde{M}_k)}$, $\tilde{M}_k$ being the model associated with the largest $p(M_k|\mathbf{Y}^*)$ for each selected *IC*. The ML estimates of log k_{ro} (i.e., log k_{ro} computed with $\hat{\boldsymbol{\theta}}$) associated with $\tilde{M}_k$ are also shown. Note that the ML estimates of log k_{ro} are very close to log k_{ro}^* in all subplots of Figure 6. This result, when considered by itself, could imbue one with an unjustified sense of confidence about the predictive capabilities of model $\tilde{M}_k$ because it does not consider the uncertainty linked to (i) the ML model parameter estimates and (ii) the model choice (when viewed in the context of a pool of alternative model possibilities). These aspects are fully included in the MLBMA. It is noted that here the model-averaging procedure has a limited effect on the average value of estimated relative permeability, i.e., $E(\mathbf{Y}|\mathbf{Y}^*) \approx E(\mathbf{Y}|\mathbf{Y}^*, \tilde{M}_k)$, consistent with the observation that $p(\tilde{M}_k|\mathbf{Y}^*) > 95\%$ for all considered cases. Otherwise, we find that the uncertainty associated with the model choice is in general not negligible, as $Var(\mathbf{Y}|\mathbf{Y}^*) > Var(\mathbf{Y}|\mathbf{Y}^*, \tilde{M}_k)$, a finding which is particularly evident when *NLL*, *BIC*, and AIC_C are considered as model-averaging criteria (see Figures 6a–6c).

The results of the corresponding analysis for experiments *W*2 are illustrated in Figure 7 for $IC = AIC_c$ (Figure 7a) and *KIC* (Figure 7b). Note that in this case *NLL* and *BIC* favor M_{10} with posterior probability equal to 1. Consistent with the results in Figure 6, we observe that $E(\mathbf{Y}|\mathbf{Y}^*) \approx E(\mathbf{Y}|\mathbf{Y}^*, \tilde{M}_k)$ while the effect of model

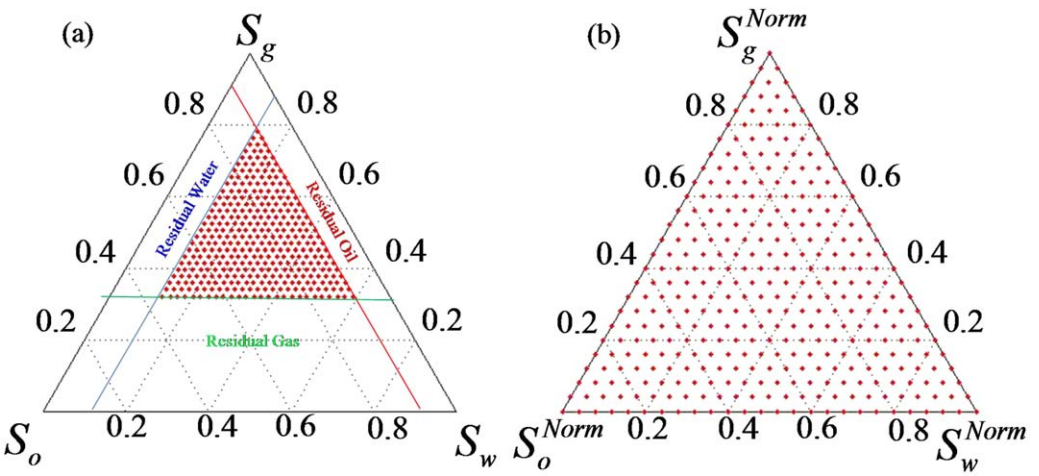

Figure 8. (a) Original and (b) reduced (normalized) saturation space. Circles represent the 351 sampling points at which eigenvectors of (18)–(19) are calculated.

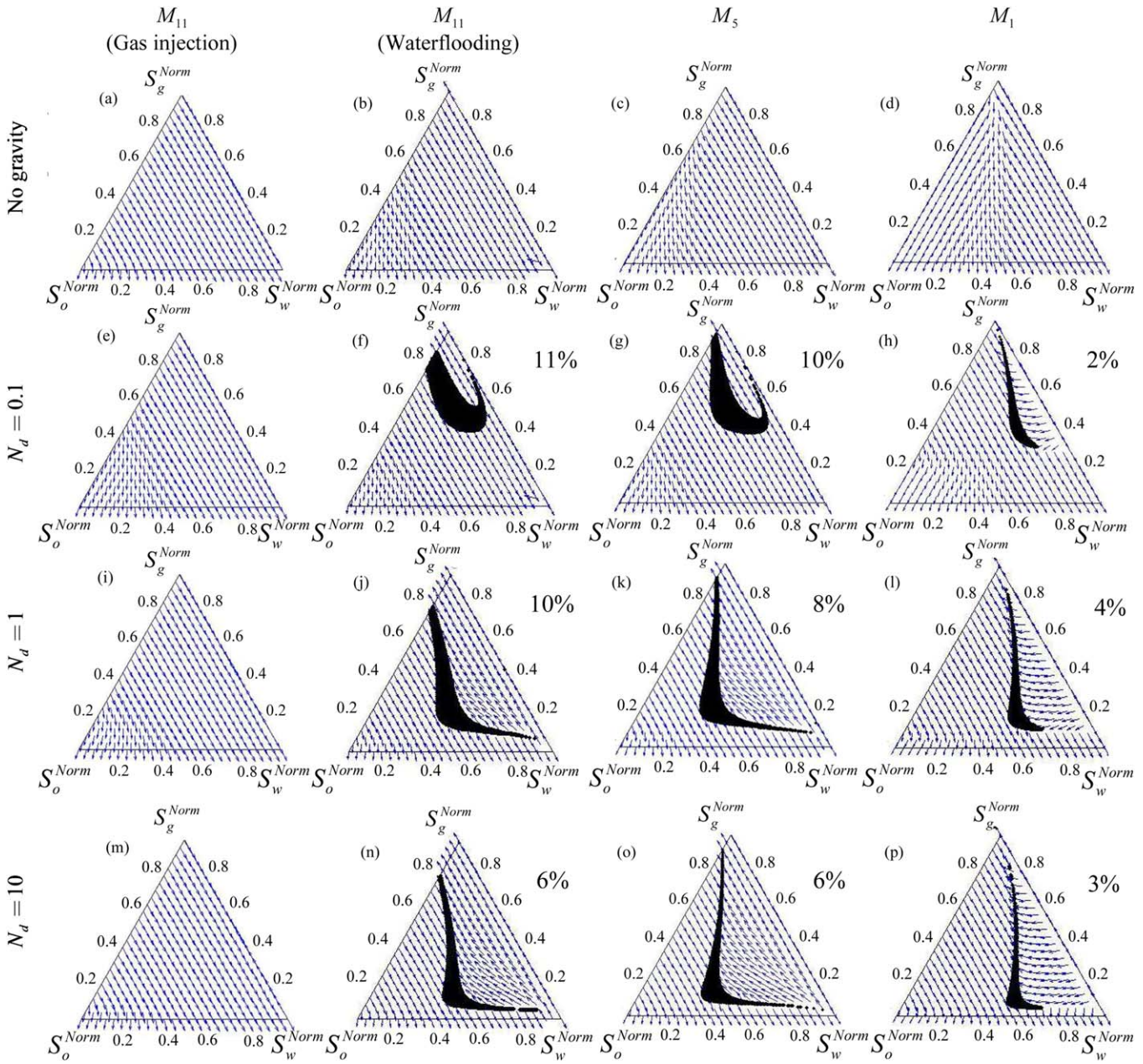

Figure 9. Distributions of eigenvectors associated with fast rarefaction waves in the reduced saturation space. Results are illustrated (a–d) in the absence and (e–p) in the presence of gravity effects with selected values of N_d. Elliptic regions are depicted as black areas. The percentage of the saturation space covered by elliptic regions is indicated where relevant.

averaging on the quantification of uncertainty is particularly important when *KIC* is considered as information criterion.

3.3. Occurrence of Elliptic Regions

Here we compare the results of our study on the occurrence of elliptic regions for (i) two classical models typically used in black-oil reservoir simulators, Stone I (M_1) and Baker (M_5), and (ii) model M_{11} which was selected as best to jointly interpret the complete data set of *Alizadeh and Piri* [2014b] in section 3.2 (see Table 2).

Figure 8a illustrates the 351 sampling points used to calculate the rarefaction paths in the saturation space. The saturation domain where elliptic regions are studied is bounded by the maximum ($\bar{S}_\alpha^M$) and residual ($\bar{S}_{r\alpha}$) saturation of fluid phase α. Figure 8b depicts the distribution of the sampling points mapped within

the ternary diagram of reduced saturations $S_\alpha^{Norm}=(S_\alpha-\bar{S}_{r\alpha})/\left(\bar{S}_\alpha^M-\bar{S}_{r\alpha}\right)$, where $\bar{S}_{r\alpha}=\bar{S}_{wc}$ for $\alpha=w$, $\bar{S}_{r\alpha}=\bar{S}_{rog}$ for $\alpha=o$, and $\bar{S}_{r\alpha}=\bar{S}_{gt}$ for $\alpha=g$ (w, o, and g, respectively, denoting water, oil, and gas). At each sampling point, we evaluate the eigenvalues (18) of the Jacobian matrix **A** (17) associated with the flow equations (12). Values of fluids viscosities and densities are taken from *Alizadeh and Piri* [2014b]. In order to have a detailed definition of the elliptic regions, when the radicand in (18) is negative (at least) at one of the 351 sampling points depicted in Figure 8a we increase the number of sampling points up to 30,000. In a water-wet system, fast rarefactions correspond to situations in which gas or/and water saturation increases (corresponding, e.g., to oil production during primary gas injection and/or secondary waterflooding), slow rarefactions being related to increasing oil saturation (corresponding, e.g., to oil generation) [*Shearer and Trangenstein*, 1989; *Jackson and Blunt*, 2002]. Here we are mainly concerned with the fast rarefactions corresponding, for example, to oil productions under WAG injection scenarios.

Figure 9 depicts the distribution of eigenvectors evaluated with the selected models and associated with fast rarefaction waves in the saturation space in the absence of gravity (Figures 9a–9d) and for three selected values of the gravity number N_d (Figures 9e–9p). Results related to M_{11} for primary gas injection (Figures 9a, 9e, 9i, and 9m) have been obtained by setting $\bar{S}_{row}=38.5\%$. Qualitatively similar results have been obtained by using diverse $\bar{S}_{row}$ values in the range $38.5\% \leq \bar{S}_{row} \leq 65\%$ (not shown).

Figures 9a–9d clearly show that the system (12) is hyperbolic within the entire saturation space when gravity forces are neglected, regardless the model selected. Use of M_{11} for primary gas injection (Figure 9a) yields eigenvectors which are mostly parallel to the gas-water edge, i.e., most of the eigenvectors are oriented along directions of constant oil saturations. The use of M_1 (Figure 9d) results in eigenvectors that rotate near the vertex $S_g^{Norm} \approx 1$ (i.e., $S_o \approx \bar{S}_{rog}$ and $S_w \approx \bar{S}_{wc}$), the latter constituting an umbilic point [*Shearer and Trangenstein*, 1989]. This umbilic point is seen to shift toward smaller S_g^{Norm} values along the oil-gas edge when M_{11} (for waterflooding) and M_5 are considered. Comparison of Figures 9b and 9c shows that implementation of M_{11} (for waterflooding) or M_5 yields very similar changes in the saturation states across the ternary diagram. This is likely related to the observation that both models are based on saturation-weighted interpolation techniques. Eigenvectors are oriented along directions of constant oil saturations for the regions of high gas content ($S_g^{Norm} \geq 0.8$) where estimates of k_{ro} are proportional to $\bar{k}_{rog}^D$ (see equation (1)).

When gravity effects are included (Figures 9e–9p), all models are characterized by the occurrence of elliptic regions, where the directions associated with the eigenvectors coincide, the only notable exception being model M_{11} for gas injection (Figures 9e, 9i, and 9m), because in this case k_{ro} evaluated through (S30) is a function of oil saturation [*Shearer and Trangenstein*, 1989]. The fraction of the saturation space covered by elliptic regions is also listed (when present) in Figures 9e–9p. We observe that the elliptic regions tend to extend to zones characterized by low gas saturations as N_d is increased from 0.1 to 1.0. A further increase of N_d does not change dramatically the shape of the elliptic regions. While the Stone I model (M_1) leads to elliptic regions which cover about 3% of the entire saturation space regardless of the value of N_d, the extent of the elliptic regions observed for M_{11} (for water injection) and M_5 tends to decrease with increasing N_d.

4. Conclusions

We analyze a suite of eleven three-phase oil relative permeability models and compare the ability of describing three-phase oil relative permeability (k_{ro}) data when (i) only two-phase data are employed and (ii) two and three-phase data are jointly used for model calibration. The study is based on a recently published data set [*Alizadeh and Piri*, 2014b] which reports data acquired in a water-wet Bentheimer sandstone sample. Our study leads to the following major conclusions.

1. The model proposed by *Ranaee et al.* [2015] (identified as M_{11} in Table 1) provides reasonably accurate estimates of k_{ro} data, supporting its ability to embed the role of hysteresis effects for the characterization of oil displacement in three-phase systems. All model selection criteria analyzed select M_{11} as the best model to interpret the considered data set, when all data (gas injection and waterflooding) are jointly considered for model parameter estimation.
2. Model M_{11} renders high-quality estimates of k_{ro} even when three-phase data are not included and the model is employed to provide predictions of three-phase relative permeabilities by relying solely on two-phase data, thus supporting its predictive capability. Remarkably, estimates of k_{ro} obtained by M_{11} solely

on the basis of two-phase data are of same or higher quality (in terms of mean square error) than their counterparts obtained with all other tested models calibrated on the basis of three-phase oil relative permeability data. On the bases of these results, additional testing of model M_{11} against experimental data is foreseen. In this context, a possible candidate database is, for example, the one recently presented by *Moghadasi et al*. [2016], or others, as they become available.

3. Multimodel analyses based on Maximum Likelihood Bayesian Model Averaging provide an efficient way of combining the predictive power of a collection of competitive k_{ro} models to render high quality results.
4. The use of the classical Stone I and Baker models induces elliptic regions when the gravity effects are included in the analysis. Employing the sigmoid-based model (M_{11}) of *Ranaee et al*. [2015] does not lead to elliptic regions under gas injection conditions, while no elliptic regions arise under waterflooding only in the absence of gravity effects. The location of elliptic regions in the saturation space tends to vary only minimally when the gravity number $1 \leq N_d \leq 10$ for these models.

Acknowledgments

Funding from the European Union's Horizon 2020 Research and Innovation program (Project "Furthering the knowledge Base for Reducing the Environmental Footprint of Shale Gas Development" FRACRISK, grant agreement 640979) is acknowledged. All data used in the paper will be retained by the authors for at least 5 years after publication and will be available to the readers upon request.

References

Alizadeh, A. H., and M. Piri (2014a), Three-phase flow in porous media: A review of experimental studies on relative permeability, *Rev. Geophys.*, *52*, 468–521, doi:10.1002/2013RG000433.

Alizadeh, A. H., and M. Piri (2014b), The effect of saturation history on three-phase relative permeability: An experimental study, *Water Resour. Res.*, *50*, 1636–1664, doi:10.1002/2013WR014914.

Baker, L. E. (1988), Three phase relative permeability correlation, paper SPE-17369 presented at Symposium on Enhanced Oil Recovery, Soc. of Pet. Eng., Tulsa, Okla.

Bianchi Janetti, E., M. Riva, and A. Guadagnini (2015), Analytical expressions for three-phase generalized relative permeabilities in water- and oil-wet capillary tubes, *Comput. Geosci.*, *20*(3), 555–565, doi:10.1007/s10596-015-9508-5.

Blunt, M. J. (2000), An empirical model for three-phase relative permeability, *SPE J.*, *5*, 435–445.

Carrera, J., and S. P. Neuman (1986), Estimation of aquifer parameters under transient and steady state conditions: 1. Maximum likelihood method incorporating prior information, *Water Resour. Res.*, *22*, 199–210.

Chukwudeme, E. A., I. Fjelde I., K. P. Abeysinghe, and A. Lohne (2014), Effect of interfacial tension on water/oil relative permeability on the basis of history matching to coreflood data, *SPE Reservoir Eval. Eng.*, *17*, 37–48.

Ciriello, V., A. Guadagnini, V. Di Federico, Y. Edery, and B. Berkowitz (2013), Comparative analysis of formulations for conservative transport in porous media through sensitivity-based parameter calibration, *Water Resour. Res.*, *49*, 5206–5220, doi:10.1002/wrcr.20395.

Ciriello, V., Y. Edery, A. Guadagnini, and B. Berkowitz (2015), Multimodel framework for characterization of transport in porous media, *Water Resour. Res.*, *51*, 3384–3402, doi:10.1002/2015WR017047.

Corey, A. T., and C. H. Rathjens (1956), Effect of stratification on relative permeability, *J. Pet. Technol.*, *8*, 69–71.

Delshad, M., and G. A. Pope (1989), Comparison of the three-phase oil relative permeability models, *Transp. Porous Med.*, *4*, 59–83.

DiCarlo, D. A., A. Sahni, and M. J. Blunt (2000), The effect of wettability on three-phase relative permeability, *Transp. Porous Med.*, *39*, 347–366.

Du, Y., O. B. Bolaji, and D. Li (2004), Literature review on methods to obtain relative permeability data, paper presented at 5th Conference and Exposition on Petroleum Geophysics, Society of Petroleum Geophysicists (SPG), Hyderabad, India.

Fatemi, S. M., M. Sohrabi, M. Jamiolahmady, S. Ireland, and G. Robertson (2011), Experimental investigation of near-miscible water-alternating-gas (WAG) injection performance in water-wet and mixed-wet systems, paper SPE-145191 presented at Offshore Europe Oil and Gas Conference and exhibition, Soc. of Pet. Eng., Aberdeen, U. K.

Fenwick, D. H., and M. J. Blunt (1998), Network modeling of three-phase flow in porous media, *SPE J.*, *3*(1), 86–96, doi:10.2118/38881-PA.

Harbert, L. W. (1983), Low interfacial tension relative permeability, paper SPE-12171 presented at 58th Annual Technical Conference and Exhibition, Soc. of Pet. Eng., San Francisco, Calif.

Hurvich C. M., and C. L. Tsai (1989), Regression and time series model selection in small samples, *Biometrika*, *76*, 297–307.

Hustad, O. S., and A. G. Hansen (1995), A consistent correlation for three-phase relative permeabilities and phase pressures based on three sets of two-phase data, *8th European Symposium on Improved Oil Recovery*, European Association of Geoscientist and Engineers (EAGE), Vienna, Austria.

Jackson, M. D., and M. J. Blunt (2002), Elliptic regions and stable solutions for three-phase flow in porous media, *Transp. Porous Med.*, *48*, 249–269, doi:10.1023/A:1015726412625.

Jerauld, G. R. (1997), General three-phase relative permeability model for Prudhoe Bay, *SPE Reservoir Eng.*, *12*, 255–263.

Juanes, R., and T.W. Patzek (2004), Relative permeabilities for strictly hyperbolic models of three-phase flow in porous media, *Transp. Porous Med.*, *57*, 125–152, doi:10.1023/B:TIPM.0000038251.10002.5e.

Kalaydjian, F. J.-M., J.-C. Moulu, O. Vizika, and P. K. Munkerud (1997), Three-phase flow in water-wet porous media: Gas/oil relative permeabilities for various spreading conditions, *J. Pet. Sci. Eng.*, *17*(3–4), 275–290, doi:10.1016/S0920-4105(96)00038-1.

Kashyap, R. L. (1982), Optimal choice of AR and MA parts in autoregressive moving average models, *IEEE Trans. Pattern Anal. Mach. Intel.*, *4*, 99–104.

Kianinejad, A., and D. A. DiCarlo (2016), Three-phase oil relative permeability in water-wet media: A comprehensive study, *Transp. Porous Med.*, *112*(3), 665–687, doi:10.1007/s11242-016-0669-z.

Kianinejad, A., X. Chen, and D. A. DiCarlo (2015), The effect of saturation path on three-phase relative permeability, *Water Resour. Res.*, *51*, 9141–9164, doi:10.1002/2015WR017185.

Lomeland, F., and E. Ebeltoft (2013), Versatile three-phase correlations for relative permeability and capillary pressure, paper presented at International Symposium of the Society of Core Analysts, The Soc. of Core Anal., Napa Valley, Calif.

Moghadasi, L., A. Guadagnini, F. Inzoli, M. Bartosek, and D. Renna (2016), Characterization of two- and three-phase relative permeability of water-wet porous media through X-ray saturation measurements, *J. Petrol. Sci. Eng.*, doi:10.1016/j.petrol.2016.05.031, in press.

Neuman, S. P. (2002), Accounting for conceptual model uncertainty via maximum likelihood Bayesian model averaging, *Acta Univ. Carol. Geol.*, *46*, 529–534.

Neuman, S. P. (2003), Maximum likelihood Bayesian averaging of alternative conceptual-mathematical models, *Stochastic Environ. Res. Risk Assess.*, *17*, 291–305, doi:10.1007/s00477-003-0151-7.
Neuman, S. P., L. Xue, M. Ye, and D. Lu (2012), Bayesian analysis of data-worth considering model and parameter uncertainties, *Adv. Water Resour.*, *36*, 75–85, doi:10.1016/j.advwatres.2011.02.007.
Nocedal, J., and S. J. Wright (2006), *Numerical Optimization*, 2nd ed., Springer, N. Y.
Oak, M. J. (1990), Three-phase relative permeability of water-wet Berea, paper SPE-20183 presented at 7th SPE/DOE Enhanced Oil Recovery Symposium, Tulsa, Okla.
Piri, M., and M. J. Blunt (2005), Three-dimensional mixed-wet random pore-scale network modeling of two and three-phase flow in porous media, I. Model description, *Phys. Rev. E*, *71*, 206–301, doi:10.1103/PhysRevE.71.026301.
Ranaee, E., G. M. Porta, M. Riva, M. J. Blunt, and A. Guadagnini (2015), Prediction of three-phase oil relative permeability through a sigmoid-based model, *J. Petrol. Sci. Eng.*, *126*, 190–200, doi:10.1016/j.petrol.2014.11.034.
Riva, M., M. Panzeri, A. Guadagnini, and S. P. Neuman (2011), Role of model selection criteria in geostatistical inverse estimation of statistical data- and model-parameters, *Water Resour. Res.*, *47*, W07502, doi:10.1029/2011WR010480.
Schwarz, G. E. (1978), Estimating the dimension of a model, *Ann. Stat.*, *6*, 461–464.
Shahverdi, H., and M. Sohrabi (2013), An improved three-phase relative permeability and hysteresis model for the simulation of a water-alternating-gas injection, *SPE J.*, *18*, 841–850.
Shearer, M., and J. A. Trangenstein (1989), Loss of real characteristics for models of three-phase flow in a porous medium, *Transp. Porous Med.*, *4*, 499–525.
Sohrabi, M., A. Danesh, and M. Jamiolahmady (2008), Visualisation of residual oil recovery by near-miscible gas and SWAG injection using high-pressure micromodels, *Transp. Porous Med.*, *74*, 239–257, doi:10.1007/s11242-007-9193-5.
Spiteri, E. J., and R. Juanes (2006), Impact of relative permeability hysteresis on the numerical simulation of WAG injection, *J. Petrol. Sci. Eng.*, *50*, 115–139, doi:10.1016/j.petrol.2005.09.004.
Stone, H. L. (1970), Probability model for estimation of three-phase relative permeability, *J. Petrol. Technol.*, *22*, 214–218.
Stone, H. L. (1973), Estimation of three-phase relative permeability and residual oil data, *J. Petrol. Technol.*, *12*, 53–61.
Suicmez, V. S., M. Piri, and M. J. Blunt (2007), Pore-scale simulation of water alternate gas injection, *Transp. Porous Med.*, *66*, 259–286, doi:10.1007/s11242-006-0017-9.
Suicmez, V. S., M. Piri, and M. J. Blunt (2008), Effects of wettability and pore-level displacement on hydrocarbon trapping, *Adv. Water Resour.*, *31*, 503–512, doi:10.1016/j.advwatres.2007.11.003.
Trangenstein, A. J. (1989), Three-phase flow with gravity, *J. Contemp. Math.*, *100*, 147–159.
Tsai, F. T. C., and X. Li. (2008), Inverse groundwater modeling for hydraulic conductivity estimation using Bayesian model averaging and variance window, *Water Resour. Res.*, *44*, W09434, doi:10.1029/2007WR006576.
Van Dijke, M. I. J., and K. S. Sorbie (2003), Pore-scale modeling of three-phase flow in mixed-wet porous media: Multiple displacement chains, *J. Petrol. Sci. Eng.*, *39*, 201–216, doi:10.1016/S0920-4105(03)00063-9.
Van Dijke, M. I. J., K. S. Sorbie, M. Sohrabi, and A. Danesh (2006), Simulation of WAG floods in an oil-wet micromodel using a 2-D pore-scale network model, *J. Petrol. Sci. Eng.*, *52*, 71–86, doi:10.1016/j.petrol.2006.03.014.
Vizika, O., and J. M. Lombard (1996), Wettability and spreading: Two key parameters in oil recovery with three-phase gravity drainage, *SPE Reservoir Eng.*, *11(1)*, 54–60, doi:10.2118/28613-PA.
Ye, M., S. P. Neuman, and P. D. Meyer (2004), Maximum likelihood Bayesian averaging of spatial variability models in unsaturated fractured tuff, *Water Resour. Res.*, *40*, W05113, doi:10.1029/2003WR002557.
Ye, M., P. D. Meyer, and S. P. Neuman (2008), On model selection criteria in multimodel analysis, *Water Resour. Res.*, *44*, W03428, doi:10.1029/2008WR006803.